Supplemental material for "Imaging crystal stress in diamond using ensembles of nitrogen-vacancy centers"

P. Kehayias,[1,2,*] M. J. Turner,[1,3] R. Trubko,[1] J. M. Schloss,[3,4]
C. A. Hart,[1] M. Wesson,[5] D. R. Glenn,[1] and R. L. Walsworth[1,2,3]

[1] *Department of Physics, Harvard University, Cambridge, MA 02138, USA*
[2] *Harvard-Smithsonian Center for Astrophysics, Cambridge, MA 02138, USA*
[3] *Center for Brain Science, Harvard University, Cambridge, MA 02138, USA*
[4] *Department of Physics, Massachusetts Institute of Technology, Cambridge, MA 02139, USA*
[5] *Department of Physics, University of Chicago, Chicago, IL 60637, USA*

CONTENTS

Full details of diamond samples investigated 1
Selected regions of Sample A 1
Summary of additional diamond samples studied 1

Spin-stress terms in the NV Hamiltonian 2
Corrections from neglected spin-stress terms 2
Stress and electric-field contributions to the NV ground-state Hamiltonian 3
$M_{z,\kappa}$ imaging using NV vector magnetic microscopy and projection magnetic microscopy 3
Alternative NV spin-stress coupling constants 4

Birefringence imaging methodology and interpretation 5
Birefringence imager setup 5
Extracting birefringence parameters 5
Birefringence-to-stress approximate model 7
Minimum detectable stress using birefringence imaging 7
Comparing birefringence and NV $M_{z,\kappa}$ measurements for Sample A 7

Strain limitations for NV magnetic and $M_{z,\kappa}$ imaging 9
Influence of $M_{z,\kappa}$ gradients on NV resonance lineshapes 9
$M_{z,\kappa}$ inhomogeneity effects on magnetic vector measurements 10
Advantages of NV $M_{z,\kappa}$ imaging 10
Advantages of birefringence imaging 11

NV $M_{z,\kappa}$ and stress maps for additional samples 11

References 12

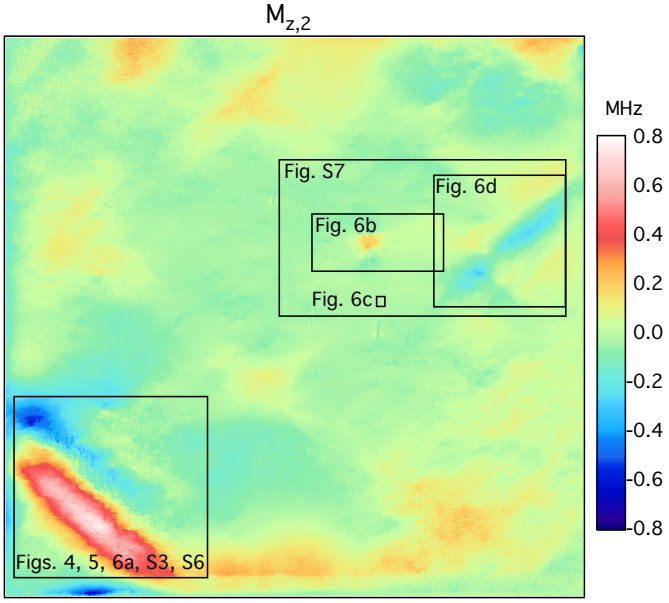
FULL DETAILS OF DIAMOND SAMPLES INVESTIGATED

Selected regions of Sample A

Figure S1 shows the regions on Sample A selected for further analysis in other figures. This displays the fields-of-view used to illustrate how different strain features affect NV magnetometry and how NV stress mapping compares to birefringence imaging.

Summary of additional diamond samples studied

Table S1 lists the properties for nine additional diamond samples we studied (labeled Sample B through Sample J), with NV layer thicknesses ranging from 20 nm to 140 μm. We include these samples to provide additional examples of various strain features. NV $M_{z,\kappa}$ and stress maps for the additional samples are included in the last section.



Supplemental Figure S1. Field-of-view locations on Sample A used for other figures in the main text and supplemental material.

Sample	Dimensions	[N] in layer	Layer Thickness	Substrate	Irradiated/ Annealed?	References
A	4×4×0.5 mm^3	25 ppm	13 μm	CVD	Yes / Yes	Studied in the main text
B	4×4×0.5 mm^3	20 ppm	4 μm	CVD	Yes / Yes	Sample D4 in Ref. [S1]
C	5×5×0.4 mm^3	10 ppm	40 μm	CVD	Yes / Yes	-
D	2×2×0.5 mm^3	2×10^{11}/cm^2 dose	20 nm	CVD	14 keV $^{14}N^+$ / Yes	Sample D1 in Ref. [S1]
E	1.7×1.5×0.5 mm^3	10 ppm	40 μm	CVD	No / No	Sample C in Ref. [S2]
F	4×4×0.3 mm^3	0.75 ppm	140 μm	HPHT	No / No	Sample B in Ref. [S2]
G	4.5×4.5×0.5 mm^3	20 ppm	4 μm	CVD	Yes / Yes	Used in Ref. [S3]
H	4×4×0.5 mm^3	27 ppm	13 μm	CVD	Yes / Yes	-
I	4×4×0.5 mm^3	7.2 ppm	0.9 μm	CVD	Yes / Yes	Sample D2 in Ref. [S4]
J	4×4×0.5 mm^3	26.8 ppm	13 μm	CVD	Yes / Yes	Sample D3 in Ref. [S1]

Supplemental Table S1. Properties of all diamond samples studied in this work. Sample F has a nitrogen-enriched chemical vapor deposition (CVD) layer grown on top of a diamond substrate made by high-pressure high-temperature (HPHT) synthesis. All other samples have electronic-grade single-crystal (ELSC) substrates grown by CVD. Sample D is a $^{14}N^+$ beam implant, and the other samples were grown with a nitrogen-rich layer.

SPIN-STRESS TERMS IN THE NV HAMILTONIAN

Corrections from neglected spin-stress terms

Using second-order perturbation theory, we estimate the potential corrections of the neglected spin-stress terms $\{M_{x,\kappa}, M_{y,\kappa}, N_{x,\kappa}, N_{y,\kappa}\}$ on the NV transition frequencies. These calculations justify disregarding these terms in our analysis, keeping only the $M_{z,\kappa}$ spin-stress term. We do this analysis for the projection magnetic microscopy case, where we measure the resonance frequencies for each NV orientation separately with $\vec{B} = B_z\hat{z}$ and $B_z \approx 1$ mT. Note that the contributions from the neglected spin-stress terms may become significant if the Zeeman effect is small in comparison, which can happen if $\vec{B}$ is largely perpendicular to the NV z-axis in a vector magnetic microscopy experiment. However, the bias magnetic fields chosen for vector magnetic microscopy generally suppress the neglected spin-stress terms to an acceptably small correction.

For the $M_{x,\kappa}$ and $M_{y,\kappa}$ spin-stress terms, the $m_s = \pm 1$ electronic sublevel energies are shifted by $\pm\frac{M_{x,\kappa}^2+M_{y,\kappa}^2}{2\gamma B_z}$ while

the $m_s = 0$ electronic sublevel is unaffected. For a typical 100 kHz spin-stress contribution, this perturbation shifts the NV transition frequencies by 200 Hz, which is a $6{\times}10^{-6}$ fractional change compared to the γB_z shift. For the spin-stress values of up to ∼1 MHz observed in this work, this perturbation shifts the NV transition frequencies by 20 kHz, which is still manageable. Note that we can make the correction from the $M_{x,\kappa}$ and $M_{y,\kappa}$ terms arbitrarily small by increasing B_z.

For the $N_{x,\kappa}$ and $N_{y,\kappa}$ spin-stress terms, the $m_s = \pm1$ electronic sublevel energies are shifted by $\frac{\pm(N_{x,\kappa}^2+N_{y,\kappa}^2)}{2(D+M_{z,\kappa}\pm\gamma B_z)}$ while the $m_s = 0$ electronic sublevel is shifted by $-\frac{N_{x,\kappa}^2+N_{y,\kappa}^2}{2(D+M_{z,\kappa}+\gamma B_z)} - \frac{N_{x,\kappa}^2+N_{y,\kappa}^2}{2(D+M_{z,\kappa}-\gamma B_z)}$. When $\gamma B_z \ll D$ and $M_{z,\kappa} \ll D$, the NV transition frequencies shift by approximately $\frac{3(N_{x,\kappa}^2+N_{y,\kappa}^2)}{2D}$ and $\frac{N_{x,\kappa}^2+N_{y,\kappa}^2}{2D}$. For a 100 kHz spin-stress contribution, this perturbation shifts the NV transition frequencies by at most 5 Hz. Note that this estimate is just for illustration, as experimental values for the d and e spin-stress coupling constants for $N_{x,\kappa}$ and $N_{y,\kappa}$ are not currently reported to our knowledge [S5, S6], though Ref. [S7] calculated estimates for them numerically. The above transition frequency correction estimates justify our rationale to neglect these spin-stress terms in our analysis.

Stress and electric-field contributions to the NV ground-state Hamiltonian

Crystal stress and electric field are often intertwined through the piezoelectric, pyroelectric, and ferroelectric effects. However, the bonds between carbon atoms in the diamond lattice are covalent bonds, meaning diamond should have no permanent or induced electric dipole moment in its unit cell. Thus, in the absence of defects, stress within diamond does not cause an electric field or vice versa, but this does not mean they are unrelated. For example, an NV center can sense an electric field from nearby charged defects, which can also cause normal stress due to lattice deformation.

From Ref. [S7], the electric-field contributions to the NV ground-state Hamiltonian are

$$\begin{aligned} H_{E,\kappa} = {} & d_{||} E_z S_{z,\kappa}^2 + d_\perp[(S_{y,\kappa}^2 - S_{x,\kappa}^2)E_x + (S_{x,\kappa}S_{y,\kappa} + S_{y,\kappa}S_{x,\kappa})E_y] \\ & + d'_\perp[(S_{x,\kappa}S_{z,\kappa} + S_{z,\kappa}S_{x,\kappa})E_x + (S_{y,\kappa}S_{z,\kappa} + S_{z,\kappa}S_{y,\kappa})E_y]. \end{aligned} \tag{S1}$$

In this expression, $\vec{E}$ is the electric field in the NV coordinate system, and $\{d_{||}, d_\perp, d'_\perp\}$ are NV ground-state electric dipole parameters [S8]. The spin-stress terms in Eq. 1 in the main text and the $\vec{E}$ terms affect the same spin terms in the NV Hamiltonian, though the former originate from a stress tensor and the latter originate from a vector electric field. When performing vector magnetic microscopy or projection magnetic microscopy with $|\vec{B}| > 1$ mT, only the $M_{z,\kappa}$ and E_z terms matter, and the off-diagonal terms can be ignored.

Because of the similarity between how $M_{z,\kappa}$ and E_z enter the NV Hamiltonian, at first glance it may be unclear whether our NV ODMR measurements are imaging inhomogeneity caused by $M_{z,\kappa}$, E_z, or both. Herein we argue that our imaging experiments are primarily sensitive to $M_{z,\kappa}$, while E_z may contribute to lineshape broadening.

Our diamond samples contain NV ensembles with equal populations oriented along opposite z directions (for example, [111] and $[\bar{1}\bar{1}\bar{1}]$). There are eight NV z directions (two for each κ). Usually the NVs pointing along opposite directions behave identically, allowing us to group them together with the same κ label. Calculating the stress tensor and the $M_{z,\kappa}$ for each NV orientation (Tab. S2) we see that the NV sub-ensembles with z-axes pointing in opposite directions have the same $M_{z,\kappa}$ and the same resonance frequencies.

Although the stress tensor contributions affect the [111] and $[\bar{1}\bar{1}\bar{1}]$ NV orientations the same way, this is not true for the E_z electric field contribution. The E_z term shifts the NV resonance frequencies by equal and opposite amounts ($\pm d_{||} E_z$) for NVs with opposite z-axes. This causes a lineshape splitting or broadening rather than a common-mode shift. We did not observe such splittings in our NV magnetic resonance spectra (Fig. 2b in the main text), though a weak E_z may contribute as a linewidth broadening. Therefore, the common-mode NV resonance frequency shifts we measure are caused by $M_{z,\kappa}$ terms only. One can imagine extracting E_z from the NV resonance linewidths, but this may be difficult because the linewidth also depends on the magnetic field inhomogeneity, $M_{z,\kappa}$ inhomogeneity, microwave power, and laser power.

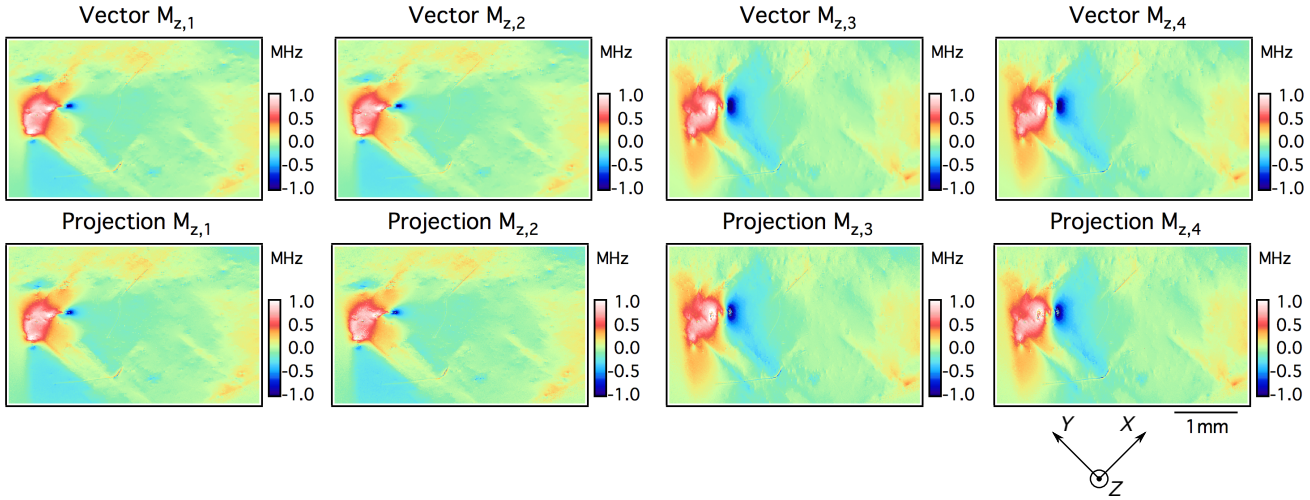
$M_{z,\kappa}$ imaging using NV vector magnetic microscopy and projection magnetic microscopy

As described in the main text, both the vector magnetic microscopy (VMM) and the projection magnetic microscopy (PMM) methods can be used to map $M_{z,\kappa}$ in a diamond [S1]. Figure S2 confirms that the VMM and PMM methods yield the same $M_{z,\kappa}$ information despite the differences between these schemes. VMM yields all $M_{z,\kappa}$ maps simultaneously without having to adjust the bias magnetic field and laser polarization angle (or rotate the diamond).

κ	NV z-axes	Stress tensors	$M_{z,\kappa}$
1	[111], [$\bar{1}\bar{1}\bar{1}$]	$\begin{pmatrix}\sigma_{XX} & \sigma_{XY} & \sigma_{XZ}\\ \sigma_{XY} & \sigma_{YY} & \sigma_{YZ}\\ \sigma_{XZ} & \sigma_{YZ} & \sigma_{ZZ}\end{pmatrix}, \begin{pmatrix}\sigma_{YY} & \sigma_{XY} & \sigma_{YZ}\\ \sigma_{XY} & \sigma_{XX} & \sigma_{XZ}\\ \sigma_{YZ} & \sigma_{XZ} & \sigma_{ZZ}\end{pmatrix}$	$a_1[\sigma_{XX}+\sigma_{YY}+\sigma_{ZZ}]$ $+2a_2[\sigma_{XY}+\sigma_{XZ}+\sigma_{YZ}]$
2	[$\bar{1}\bar{1}$1], [11$\bar{1}$]	$\begin{pmatrix}\sigma_{XX} & \sigma_{XY} & -\sigma_{XZ}\\ \sigma_{XY} & \sigma_{YY} & -\sigma_{YZ}\\ -\sigma_{XZ} & -\sigma_{YZ} & \sigma_{ZZ}\end{pmatrix}, \begin{pmatrix}\sigma_{YY} & \sigma_{XY} & -\sigma_{YZ}\\ \sigma_{XY} & \sigma_{XX} & -\sigma_{XZ}\\ -\sigma_{YZ} & -\sigma_{XZ} & \sigma_{ZZ}\end{pmatrix}$	$a_1[\sigma_{XX}+\sigma_{YY}+\sigma_{ZZ}]$ $+2a_2[\sigma_{XY}-\sigma_{XZ}-\sigma_{YZ}]$
3	[$\bar{1}$1$\bar{1}$], [1$\bar{1}$1]	$\begin{pmatrix}\sigma_{XX} & -\sigma_{XY} & \sigma_{XZ}\\ -\sigma_{XY} & \sigma_{YY} & -\sigma_{YZ}\\ \sigma_{XZ} & -\sigma_{YZ} & \sigma_{ZZ}\end{pmatrix}, \begin{pmatrix}\sigma_{YY} & -\sigma_{XY} & -\sigma_{YZ}\\ -\sigma_{XY} & \sigma_{XX} & \sigma_{XZ}\\ -\sigma_{YZ} & \sigma_{XZ} & \sigma_{ZZ}\end{pmatrix}$	$a_1[\sigma_{XX}+\sigma_{YY}+\sigma_{ZZ}]$ $+2a_2[-\sigma_{XY}+\sigma_{XZ}-\sigma_{YZ}]$
4	[1$\bar{1}\bar{1}$], [$\bar{1}$11]	$\begin{pmatrix}\sigma_{XX} & -\sigma_{XY} & -\sigma_{XZ}\\ -\sigma_{XY} & \sigma_{YY} & \sigma_{YZ}\\ -\sigma_{XZ} & \sigma_{YZ} & \sigma_{ZZ}\end{pmatrix}, \begin{pmatrix}\sigma_{YY} & -\sigma_{XY} & \sigma_{YZ}\\ -\sigma_{XY} & \sigma_{XX} & -\sigma_{XZ}\\ \sigma_{YZ} & -\sigma_{XZ} & \sigma_{ZZ}\end{pmatrix}$	$a_1[\sigma_{XX}+\sigma_{YY}+\sigma_{ZZ}]$ $+2a_2[-\sigma_{XY}-\sigma_{XZ}+\sigma_{YZ}]$

Supplemental Table S2. Stress tensors and $M_{z,\kappa}$ terms for each NV orientation, calculated using the coordinate systems used in Fig. 2a of the main text, and also in Tab. 1 of Ref [S6].

PMM is optimized for measuring one $M_{z,\kappa}$ at a time, and the procedures for lineshape fitting and $M_{z,\kappa}$ extraction are simpler [S1]. As a further check, we rotated the diamond chip by 90° about the Z-axis. The resulting $M_{z,\kappa}$ and stress maps were consistent with the unrotated maps, transforming as expected for a 90° rotation.



Supplemental Figure S2. A comparison of $M_{z,\kappa}$ maps for X-shaped defects in Sample B obtained using vector magnetic microscopy (VMM) and projection magnetic microscopy (PMM). We varied the laser polarization angle and the bias magnetic field in between measurements, keeping the diamond region constant.

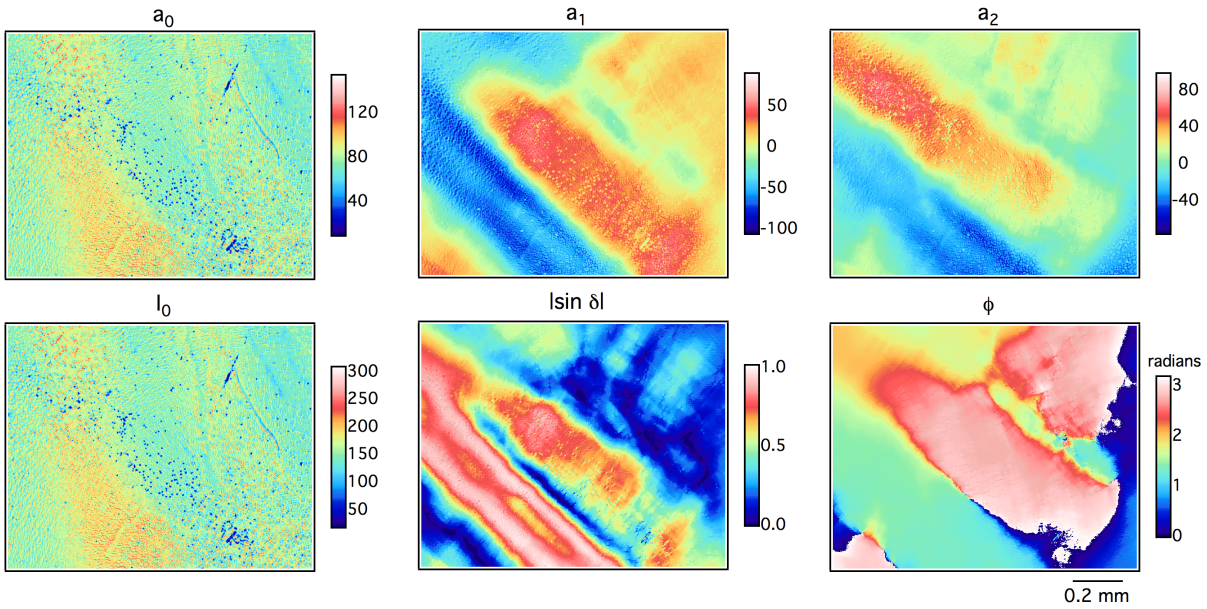
Alternative NV spin-stress coupling constants

We recently became aware of another set of experimental spin-stress coupling constants $\{a_1, a_2\} = \{11.7, -6.5\}$ MHz/GPa reported in Ref. [S6], which differ from the $\{a_1, a_2\} = \{4.86, -3.7\}$ MHz/GPa in Ref. [S5] by roughly a factor of 2. Recalculating the stress maps for our diamond samples using the values of Ref. [S6] produced visually similar stress maps. Furthermore, the calculation in Ref. [S7] reports a third set of $\{a_1, a_2\} = \{2.66, -2.51\}$ MHz/GPa. We do not include stress maps derived from these alternate $\{a_1, a_2\}$ values, though these can be provided upon request. Note that we adopt the convention used in Ref. [S5], where a positive σ_{ii} adds a positive contribution to $M_{z,\kappa}$. While we are unable to resolve the disagreement in spin-stress coupling constants, the qualitative messages of our work are unaffected.

BIREFRINGENCE IMAGING METHODOLOGY AND INTERPRETATION

Birefringence imager setup

As illustrated in Fig. 1 in the main text, our NV $M_{z,\kappa}$ imager also includes birefringence imaging capabilities. For birefringence measurements, light from a white LED illuminator passes through a 532 nm bandpass filter and a linear polarizer mounted to a motorized rotation stage before illuminating the diamond sample. The light transmitted through the birefringent diamond is collected by a 4× or 10× microscope objective. The light then passes through a circular analyzer consisting of a zero-order $\lambda/4$ wave plate aligned at 45° to a linear polarizer. The transmitted light is imaged with a CMOS camera through an eyepiece lens. We save camera images while sweeping the polarizer rotation angle α_i through 180°, usually in 10° steps. To alternate between birefringence and NV $M_{z,\kappa}$ imaging, we swap between the circular analyzer and the long-pass filter before the camera.



Supplemental Figure S3. Complete birefringence maps for Sample A.

Extracting birefringence parameters

Here we summarize the equations describing rotating-polarizer birefringence measurements, derived in Refs. [S9, S10]. The transmission intensity I_i for polarizer angle α_i is

$$I_i = \frac{1}{2} I_0 [1 + \sin 2(\alpha_i - \phi) \sin \delta], \tag{S2}$$

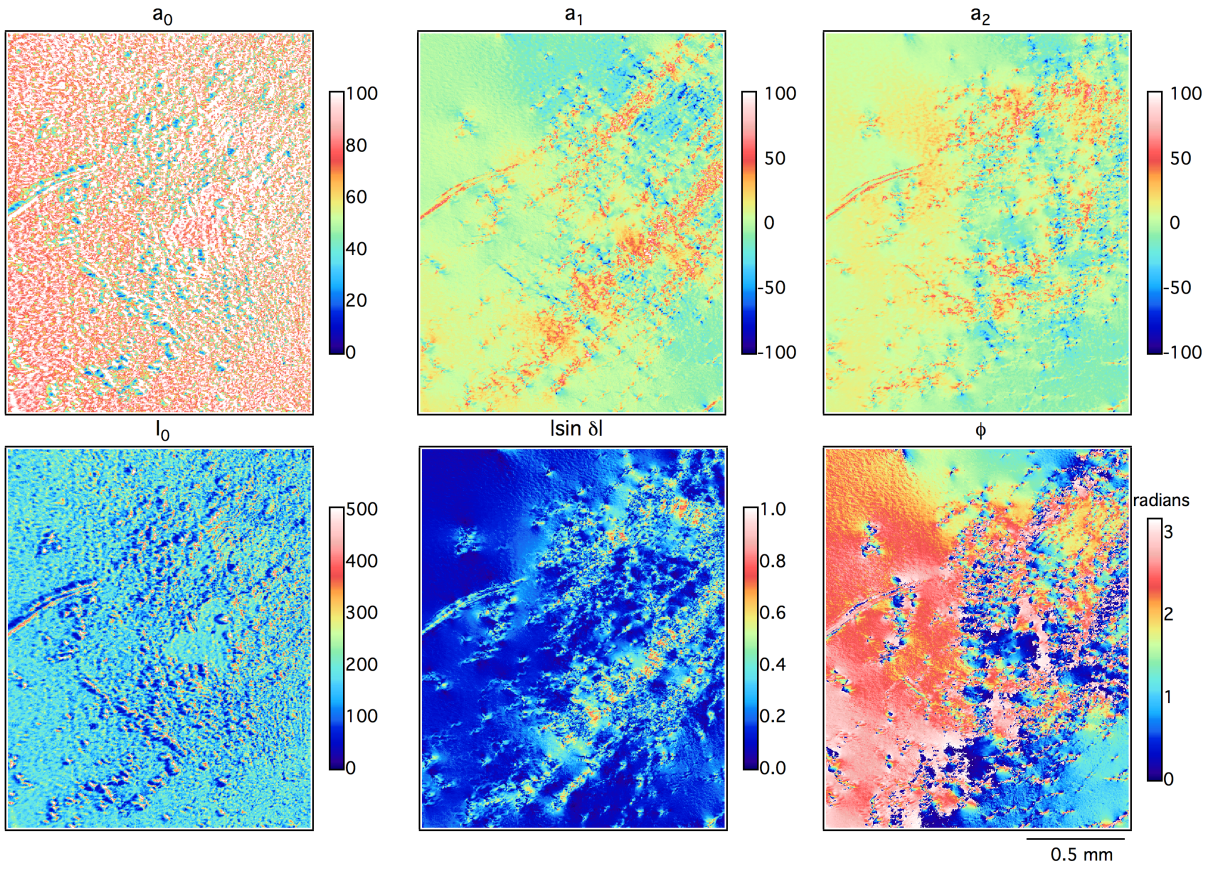
where I_0 and I_i are the initial and transmitted intensities, ϕ is the retardance orientation angle, $\delta = \frac{2\pi}{\lambda} \Delta n L$ is the optical retardance phase, and α_i is the angle of the first polarizer. This equation can be rewritten in a more convenient form

$$I_i = a_0 + a_1 \sin 2\alpha_i + a_2 \cos 2\alpha_i, \tag{S3}$$

$$a_0 = \frac{1}{2} I_0, \tag{S4}$$

$$a_1 = \frac{1}{2} I_0 \sin \delta \cos 2\phi, \tag{S5}$$

$$a_2 = -\frac{1}{2} I_0 \sin \delta \sin 2\phi. \tag{S6}$$



Supplemental Figure S4. Complete birefringence maps for Sample C.

Solving for the optical parameters of interest yields

$$I_0 = 2a_0, \tag{S7}$$

$$|\sin\delta| = \frac{({a_1}^2 + {a_2}^2)^{\frac{1}{2}}}{a_0}, \tag{S8}$$

$$\phi = \frac{\pi}{2} + \frac{1}{2}\mathrm{sgn}(a_2)\arccos\left[\frac{-a_1}{({a_1}^2 + {a_2}^2)^{\frac{1}{2}}}\right]. \tag{S9}$$

One way to extract a_0, a_1, and a_2 from a series of images with varying α_i is to fit intensities in each pixel with Eq. S3. However, this strategy is computationally intensive, especially when imaging over many pixels in a large field of view. Stepping α_i through N equal angles, we can exploit trigonometric properties to write the expressions below as a sum over the angles from $\alpha_1 = 180°/N$ to $\alpha_{\max} = 180°$:

$$a_0 = \frac{1}{N}\sum_{i=1}^{N} I_i, \tag{S10}$$

$$a_1 = \frac{2}{N}\sum_{i=1}^{N} I_i \sin 2\alpha_i, \tag{S11}$$

$$a_2 = \frac{2}{N}\sum_{i=1}^{N} I_i \cos 2\alpha_i, \tag{S12}$$

$$\alpha_1 = 180°/N, \quad \alpha_{\max} = 180°. \tag{S13}$$

Figures S3 and S4 include examples of this reconstruction procedure for $N = 18$ with Samples A and C.

Birefringence-to-stress approximate model

In order to roughly test the agreement between birefringence imaging and NV stress imaging, we use the photo-elastic equation to convert Δn to a stress (or strain) value. The stress and strain inhomogeneity through the diamond is linearly proportional to the Δn we measure [S11–S13]. Following these references, we assume an isotropic stress-optic coefficient, q_{iso}, and relate stress to Δn via

$$|\Delta n| \sim \frac{3}{4} n^3 q_{iso} \sigma \text{ and } |\Delta n| = \frac{|\delta|\lambda}{2\pi L}. \tag{S14}$$

Here $q_{iso} \approx (q_{11} - q_{22}) \approx q_{44} = 0.301 \times 10^{-12}$ Pa^{-1} [S13], $n = 2.42$ is the diamond refractive index [S14], L is the diamond thickness, λ is the optical wavelength, and $|\delta|$ is magnitude of the optical retardance phase from $|\sin\delta|$.

Solving for σ yields

$$|\sigma| \sim \frac{2}{3\pi} \frac{|\delta|\lambda}{L n^3 q_{iso}}. \tag{S15}$$

A phase accumulation of $|\delta| = \pi/2$ gives $|\sigma| \sim 85$ MPa, which is the maximum stress we can measure without order ambiguity for an optical path length of 500 μm.

Minimum detectable stress using birefringence imaging

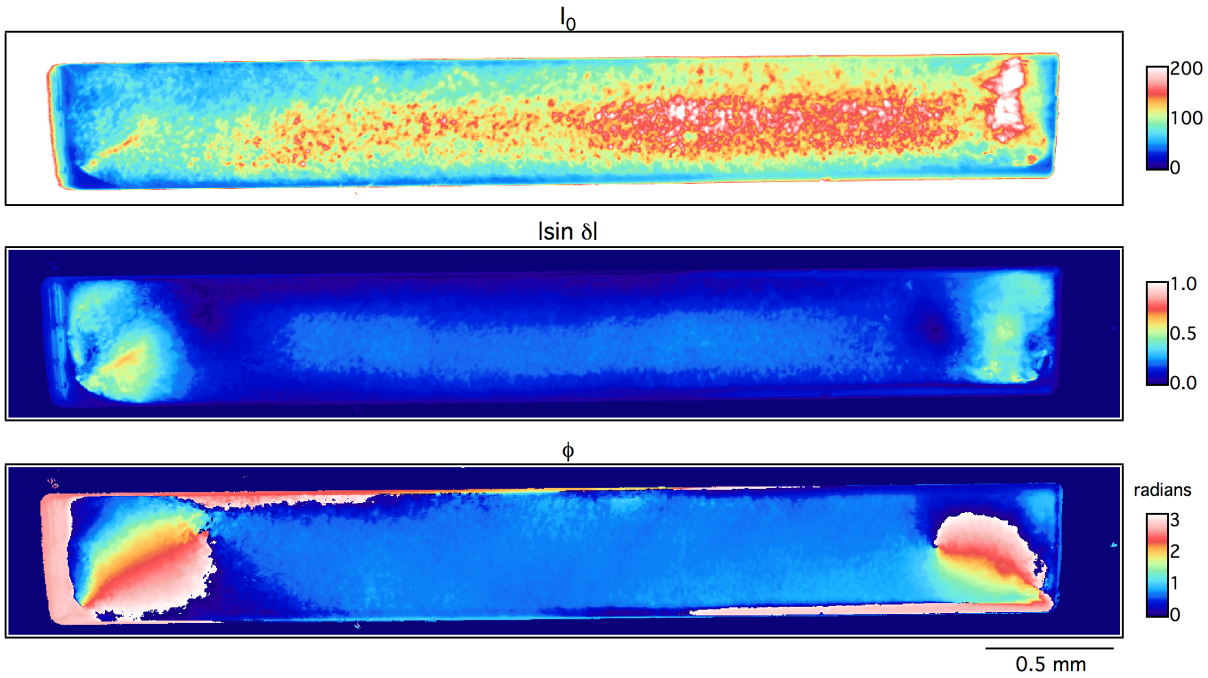
The above method can yield a rough estimate for the minimum detectable stress using birefringence. A well-optimized system can detect down to $|\sin\delta| \approx 0.001$ [S10]. This gives an approximate [S11, S13] minimum stress detected using the isotropic photo-elastic constants and assuming a constant stress throughout the 500 μm thickness of diamond of ∼0.1 MPa. More generally, we can write this as 50 MPa· μm for an arbitrary optical path length through the sample thickness. This value is typically limited by optical element quality, optical alignment, and employed calibration schemes. In our birefringence imager we can detect a minimum of $|\sin\delta| \approx 0.005$, giving a minimum-detectable stress of 0.5 MPa (250 MPa· μm). This value is limited by the employed optical elements, LED illumination power, and residual misalignment of the circular analyzer.

Comparing birefringence and NV $M_{z,\kappa}$ measurements for Sample A

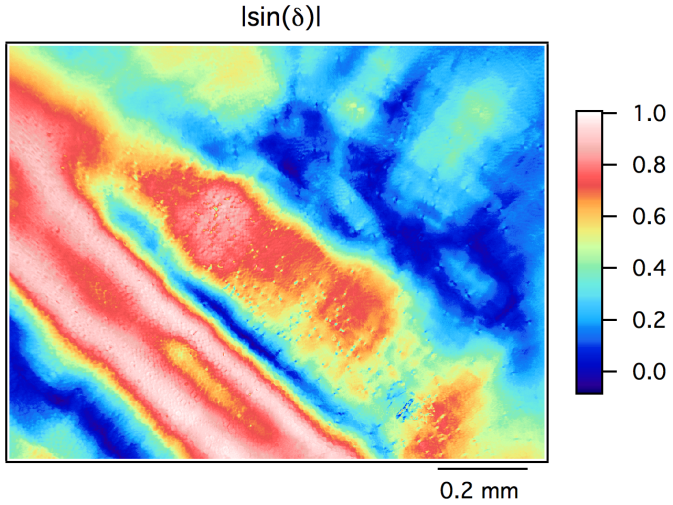
We used Sample A for a quantitative comparison of stress magnitudes generated using the NV $M_{z,\kappa}$ and optical birefringence methods. This sample contains regions which adequately fulfill the approximations needed for the rough isotropic model. It displays a relatively uniform spatial strain pattern in the X-Y imaging plane. Furthermore, Sample A is polished on its top and bottom faces and one of its side faces. This allows us to partially image its birefringence through the sides of the diamond. These measurements, shown in Fig. S5, show a generally uniform depth distribution of strain, validating the use of the birefringence-to-stress approximate model above.

One of the current limitations of the birefringence method is order ambiguity in the measurement of $|\sin\delta|$. For high-strain regions, the accumulated phase difference through the sample thickness is greater than $\pi/2$, leading to ambiguity when calculating δ and stress from $|\sin\delta|$. As described above, the maximum stress magnitude is ∼85 MPa for $L = 500$ μm and $\lambda = 532$ nm (Eq. S15). To unambiguously determine the stress magnitude from birefringence in samples with larger stress would require thinner (smaller L) samples or alternative methods [S15]. An example of this type of phase ambiguity can be seen for a sample region of interest in Sample A shown in Fig. S6 (the diagonal red stripe on the left side of the image) where $|\sin\delta|$ reaches its maximum value of 1 before decreasing in the middle of the stripe.

Figure S7 compares the birefringence map with the NV σ_{XY} map for a petal-shaped strain defect. The birefringence data is plotted as $\sin^{-1}(|\sin\delta|)$ to make all images linear in the strain amplitude. Although both images show a strain feature with four lobes, the shapes are qualitatively dissimilar, with one rotated 45° with respect to the other. The lobe orientations in the $|\sin\delta|$ map are consistent with a dislocation bundle [S16]. In birefringence imaging and X-ray topography studies from Ref. [S17] dislocation bundles were found to diverge as they propagated through the diamond thickness. Such divergence may explain the difference in the spatial structure observed between the $|\sin\delta|$ map, which is integrated over the full 500 μm thickness, and the σ_{XY} map, which shows stress in only the top 13 μm of the diamond (Fig. S7). In addition to the large petal feature, we also observe smaller petal defects in the

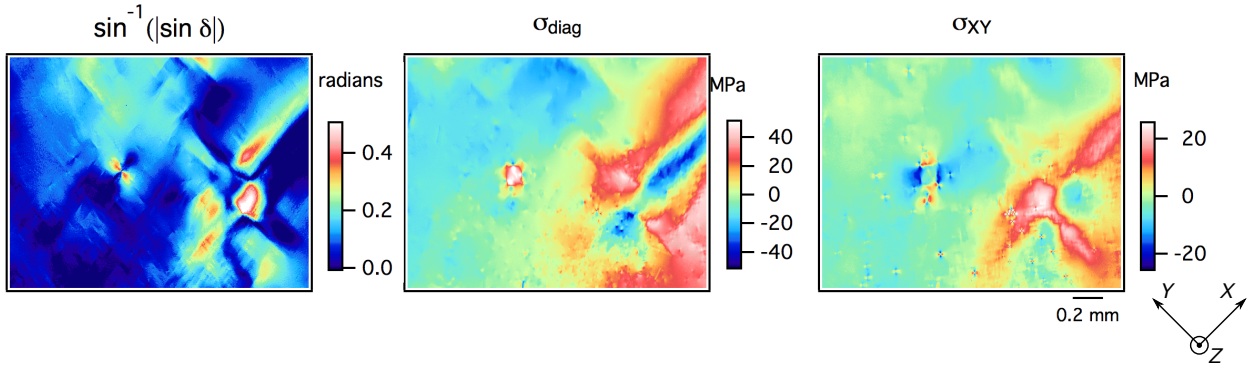


Supplemental Figure S5. Birefringence maps measured through a side face of Sample A. The speckle in the transmission image is due to one of the edges of the diamond in the optical path not being polished. This limits what can be quantitatively said about the distribution of strain, however, sources can be roughly localized. The stripe in the lower-left corner of Fig. 3 is on the left side of the image.

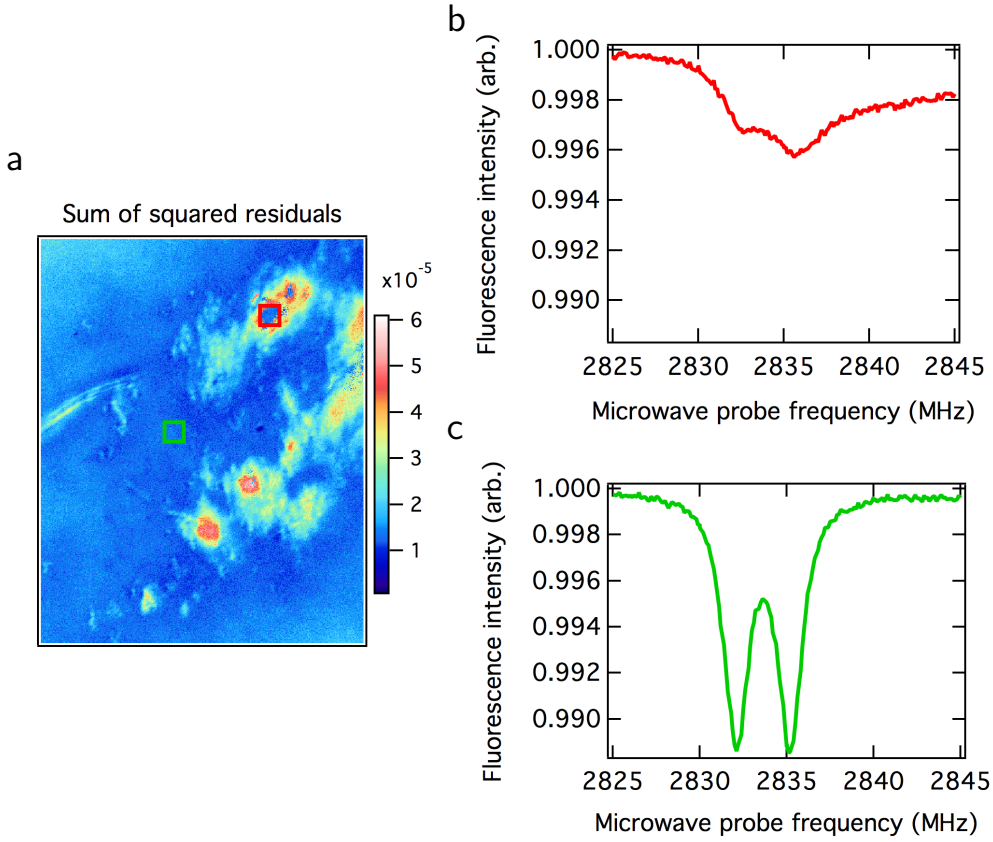


Supplemental Figure S6. A $|\sin\delta|$ birefringence map for a diagonal stripe strain defect in Sample A (see Fig. 4 in the main text). Despite the order ambiguity, the maximum stress measured using the birefringence and the $M_{z,\kappa}$ imaging techniques are consistent.

σ_{XY} maps that are not present in the birefringence maps. These features likely originate at the interface of the 13 µm thick N-doped layer with the diamond substrate; the short vertical extent of these features put them below the birefringence sensitivity limit.



Supplemental Figure S7. A zoomed-in region on Sample A showing a large petal-shaped defect originating from a dislocation bundle, imaged with birefringence and NV $M_{z,\kappa}$ imaging. The NV measurement is only sensitive to the stress in a 13 µm layer, and shows some smaller petal-shaped defects not observed the birefringence measurement.



Supplemental Figure S8. (a) Sum of squared residuals for a region of Sample C. (b)-(c) ODMR lineshapes for the $m = 0$ to -1 transition for a high-strain (red) and low-strain (green) region. The locations of these regions within the image are represented in (a) with red and green boxes. In addition to causing lineshape broadening, the strain gradient in each pixel leads to worse fit residuals. Each NV resonance is split into two lines due to hyperfine interactions with the spin-1/2 ^{15}N nucleus.

STRAIN LIMITATIONS FOR NV MAGNETIC AND $M_{z,\kappa}$ IMAGING

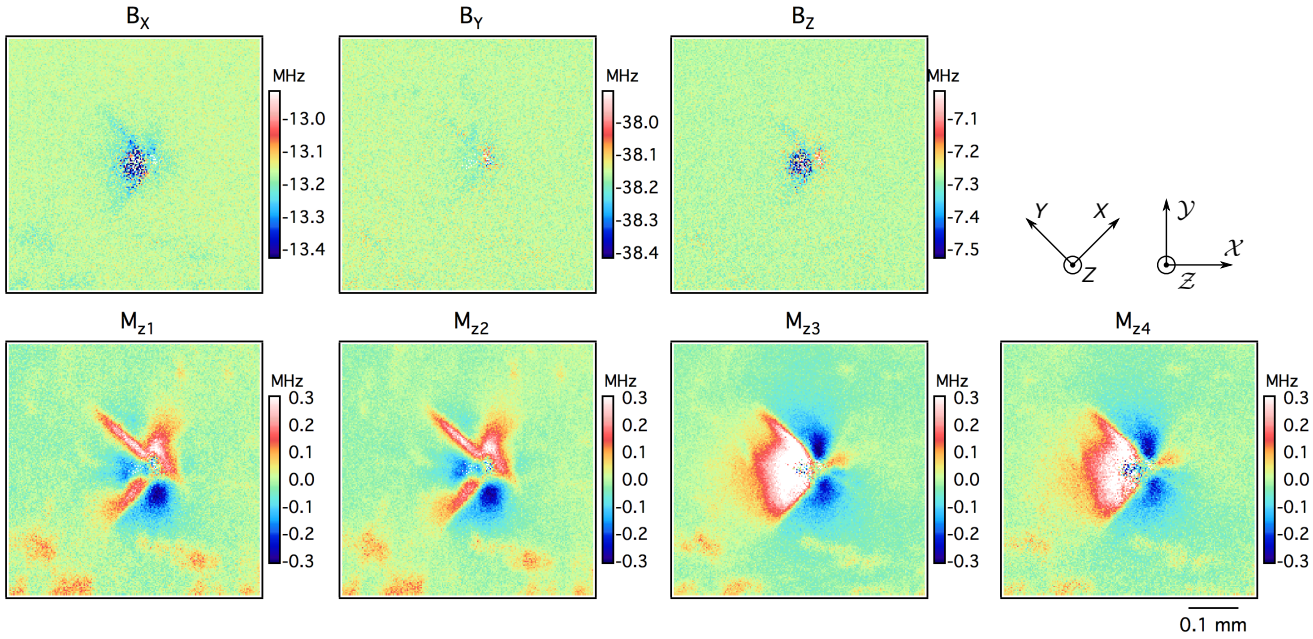
Influence of $M_{z,\kappa}$ gradients on NV resonance lineshapes

As shown in Fig. S8, $M_{z,\kappa}$ gradients can distort the single-pixel ODMR spectra, making lineshape fitting more difficult. For large gradients, the Lorentzian fit functions we use to extract the ODMR center frequencies may not describe the $M_{z,\kappa}$-broadened lineshapes accurately, potentially causing strain features to appear as systematic errors

in the magnetic images. The strain gradients within each pixel in Sample C lead to worse fit residuals (suggesting that a Lorentzian fit function is not the best choice), and also cause lineshape broadening. Ideally the single-pixel $M_{z,\kappa}$ inhomogeneity should be small compared to the other factors that determine the NV resonance linewidth (magnetic inhomogeneity, microwave field strength, and laser intensity), which is often ∼1 MHz full width at half maximum.

$M_{z,\kappa}$ inhomogeneity effects on magnetic vector measurements

To further emphasize the importance of mapping and minimizing strain in the diamond, Fig. S9 shows $M_{z,\kappa}$ maps for a lattice defect in Sample D, along with the corresponding vector magnetic images in the presence of a spatially-uniform bias magnetic field. Although the magnetic map should be homogeneous, the strain defect appears as a false magnetic feature. The false feature may be caused by covariance between fit parameters (fluorescence contrasts, resonance linewidths, and resonance frequencies) or by the $M_{z,\kappa}$ inhomogeneity distorting the ODMR lineshapes. This pathological example shows how the $M_{z,\kappa}$ imaging technique allows identification and rejection of magnetic features caused by strain, while also emphasizing the value of diamond samples with homogeneous stress/strain for NV magnetic imaging.



Supplemental Figure S9. Zoomed-in image of the $M_{z,\kappa}$ maps for a lattice defect feature in Sample D, together with the vector magnetic field maps from the same experiment in the presence of a spatially-uniform bias magnetic field. All color scales are in MHz (divide by 28.03 GHz/T for magnetic maps in tesla). The coordinates for $\{B_{\mathcal{X}}, B_{\mathcal{Y}}, B_{\mathcal{Z}}\}$ correspond to the diamond chip coordinate system $\{\mathcal{X}, \mathcal{Y}, \mathcal{Z}\}$, which is rotated by 45° from the $\{X, Y, Z\}$ unit cell coordinate system used for the stress maps. This example shows how a sufficiently large stress inhomogeneity can generate a false magnetic feature.

Advantages of NV $M_{z,\kappa}$ imaging

Here we discuss technical advantages of NV $M_{z,\kappa}$ imaging over birefringence imaging.

- An NV $M_{z,\kappa}$ imager measures the stress within the microscope depth-of-field, localizing the depth to within few micrometers in the optical diffraction limit or up to a few nanometers in a shallow nitrogen implant or delta-doped layer [S18]. A birefringence imager integrates optical retardance through the entire diamond thickness (typically hundreds of micrometers), making depth information difficult to assess.

- Since optical retardance increases with diamond thickness, birefringence imaging can be difficult for thin diamonds (30 μm thickness). Similarly, order ambiguity complicates analysis of birefringence measurements with thick diamond samples when $|\delta| > \pi/2$.

- Extracting Δn and stress from a birefringence image requires knowledge of n and L. Other polarization effects like circular birefringence can lead to incorrect conclusions about the magnitude of the linear birefringence [S19].

- While a birefringence measurement is useful for qualitative comparisons and phenomenology, an NV $M_{z,\kappa}$ measurement is more quantitative and easier to interpret. Interpreting Δn information into an absolute stress or strain is model dependent [S11].

- With a birefringence imager, the extracted optical retardance depends on the illumination wavelength(s), polarizer orientations, and birefringence in other optical components or glass. An NV $M_{z,\kappa}$ imager avoids these complications, such that measured stress inhomogeneity maps should be independent of the fluorescence microscope employed.

- Detecting whether a diamond is uniformly compressed or dilated with a birefringence measurement is challenging. An NV $M_{z,\kappa}$ measurement would see compression and dilation as a uniform shift of all four $M_{z,\kappa}$ parameters [S20]. Similarly, while $M_{z,\kappa}$ images yield all shear stress terms, birefringence imaging is only sensitive to σ_{XY} shear terms (in the plane perpendicular to the optical axis) for a given measurement [S21].

- NV $M_{z,\kappa}$ imaging requires optical access from one polished side of the diamond. Birefringence imaging requires an uninterrupted optical path through the diamond, which may be impossible if the diamond is mounted on an opaque substrate or if the back surface is too rough.

Advantages of birefringence imaging

In spite of the above drawbacks, birefringence imaging may be preferable under certain circumstances.

- Birefringence imaging is a faster experiment; it requires at minimum a single camera image (or a few images if using multiple waveplate orientations). An NV $M_{z,\kappa}$ measurement needs a few hundred camera images (roughly 50 microwave probe frequencies per NV frequency). In addition, obtaining a sufficient signal-to-noise ratio to fit the NV ODMR lineshape in each pixel usually requires averaging. This makes birefringence imaging useful for quickly characterizing diamond substrates.

- A birefringence measurement has one main parameter to optimize before measuring: namely, the $\lambda/4$ waveplate and linear polarizer should be maintained at 45° with respect to one another. For an NV experiment, the laser polarization, microwave field, and bias magnetic field must all be optimized.

- Just as strain inhomogeneity can complicate an NV magnetic microscopy experiment, magnetic field inhomogeneity can complicate an NV $M_{z,\kappa}$ experiment. A birefringence experiment is insensitive to magnetic fields.

- NV $M_{z,\kappa}$ imaging is difficult in diamonds with low NV density, broad ODMR linewidths, or weak fluorescence contrast. One example of low-NV diamonds are the high-purity diamond samples used as substrates for growth of nitrogen-enriched layers. It is imperative that these seed diamonds contain low strain inhomogeneity, as strain defects tend to propagate into the nitrogen-enriched layer. Birefringence imaging is a more fitting choice to characterize strain in such high-purity diamonds.

- In diamonds with a thick NV layer (compared to the microscope depth-of-field), fluorescence light from out-of-focus NVs can enter the microscope, complicating the ODMR $M_{z,\kappa}$ interpretation and potentially blurring the $M_{z,\kappa}$ map. This phenomenon is visible in Sample C, where the stress maps are blurred by the 40 μm NV layer when compared to the birefringence measurements.

NV $M_{z,\kappa}$ AND STRESS MAPS FOR ADDITIONAL SAMPLES

Figures S10-S19 include the complete NV $M_{z,\kappa}$ and stress maps for all diamond samples studied in this work (Samples A through J). Table S1 lists the properties of these diamonds. Here we comment on the strain features seen in each sample.

- Sample B has mm-sized X-shaped strain features present in the σ_{diag} and σ_{XY} maps (also seen in Fig. S2).

- Sample C has a 40 μm NV layer, which can degrade the NV stress mapping spatial resolution if the camera collects fluorescence from the entire NV layer. Comparing Fig. S4 and Fig. S12, if the NV layer is thicker than the typical strain feature size, the birefringence maps may yield a sharper strain image. Sample C is unique in that it has a comparable inhomogeneity in all of the stress components throughout the entire 2D layer, which could be caused by mechanical polishing and etching.

- Sample D is a nitrogen ion ($^{14}N^{+}$) implant diamond. This sample was cut from a larger diamond chip along the left and bottom edges, which exhibit less broad-scale plastic deformation than the original (top and right) edges. This sample also has some finer-scale strain inhomogeneity along the bottom edge.

- Sample E has strain inhomogeneity caused by petal-shaped defects, broad-scale plastic deformation, and a relatively homogeneous region in the middle of the sample. A larger sample was laser-cut into quarters, one piece of which is Sample E. This piece has less stress near the middle and at the cut edges (right and bottom) than at the uncut edges (left and top).

- Sample F has undergone a fracture on the right side of the image (a broken corner, see Fig. 1c in Ref. [S2]). Having strain and broad-scale plastic deformation associated with sharp corners, edges, and fractures is to be expected. The pixels in the top right have a $M_{z,\kappa}$ gradient large enough to prevent lineshape fitting using our standard fit function, and are set to zero in this image. The $M_{z,\kappa}$ values are more homogeneous toward the diamond chip interior. The σ_{XZ} and σ_{YZ} stress contributions are smaller compared to the σ_{diag} and σ_{XY} contributions, but still include some fine-scale features.

- Sample G has square etch pits [S17] and irregularly-shaped indentations on the diamond surface. These surface imperfections can come from preferential etching of lattice dislocation tracks or from damage due to mechanical polishing, and can therefore be considered as symptoms or indicators of diamond strain. The irregularly-shaped surface indentations are correlated with diamond stress (mostly in σ_{diag} and σ_{XY}).

- Sample H has diagonal streaks in the strain maps. Note that due to suboptimal experimental conditions the $M_{z,\kappa}$ and stress maps include some ripple artefacts, which are correlated with the inhomogeneous laser illumination. Fortunately, the ripple artefacts do not affect the stress maps significantly.

- Sample I has several mm-sized X-shaped strain features, similar to those seen in other samples.

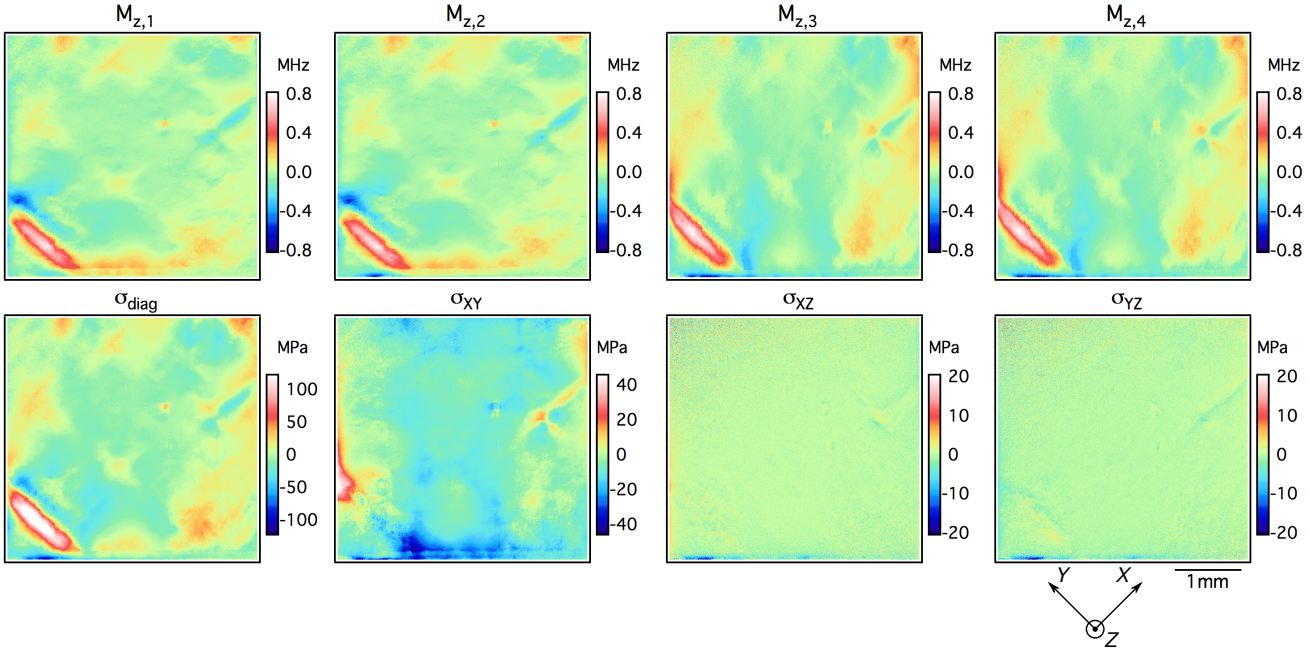
- Sample J has $M_{z,\kappa}$ and stress inhomogeneity from diagonal stripes and from the top and left edges.

---

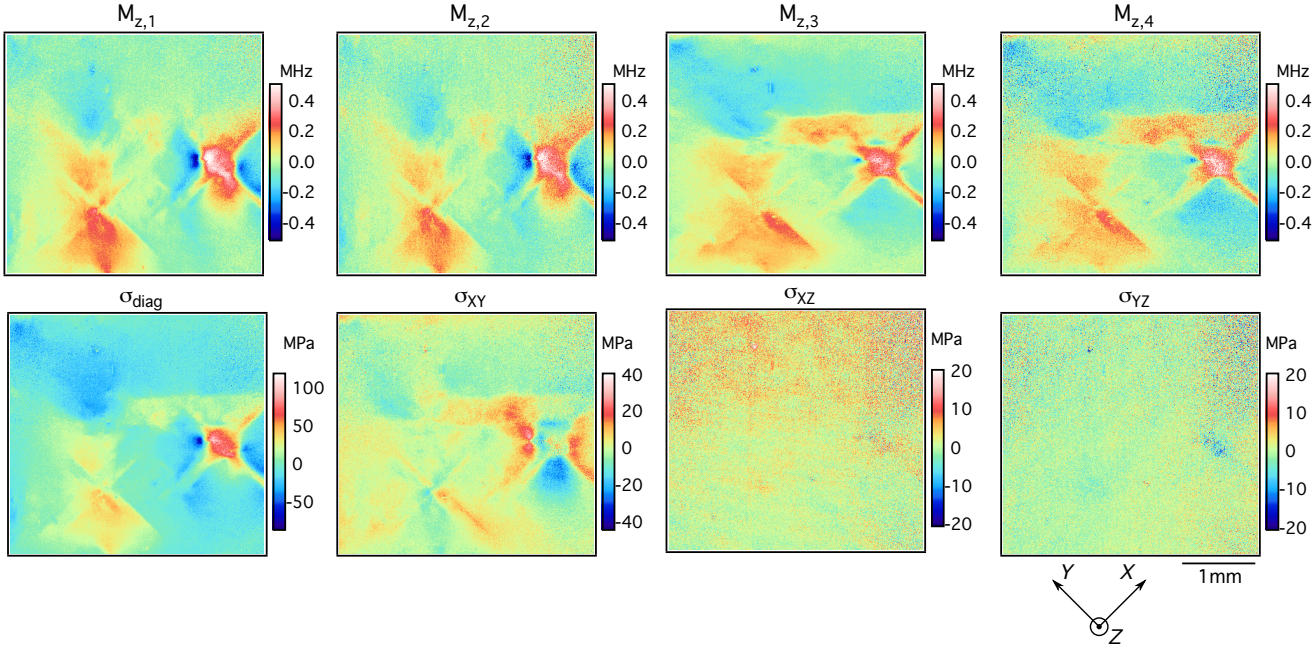
* Current address: Sandia National Laboratories, Albuquerque, NM 87123, USA

[S1] D. R. Glenn, R. R. Fu, P. Kehayias, D. Le Sage, E. A. Lima, B. P. Weiss, and R. L. Walsworth, Geochemistry, Geophysics, Geosystems **18**, 3254 (2017).
[S2] E. Bauch, C. A. Hart, J. M. Schloss, M. J. Turner, J. F. Barry, P. Kehayias, S. Singh, and R. L. Walsworth, Phys. Rev. X **8**, 031025 (2018).
[S3] H. C. Davis, P. Ramesh, A. Bhatnagar, A. Lee-Gosselin, J. F. Barry, D. R. Glenn, R. L. Walsworth, and M. G. Shapiro, Nature Communications **9**, 131 (2018).
[S4] M. P. Backlund, P. Kehayias, and R. L. Walsworth, Phys. Rev. Applied **8**, 054003 (2017).
[S5] M. S. J. Barson, P. Peddibhotla, P. Ovartchaiyapong, K. Ganesan, R. L. Taylor, M. Gebert, Z. Mielens, B. Koslowski, D. A. Simpson, L. P. McGuinness, J. McCallum, S. Prawer, S. Onoda, T. Ohshima, A. C. Bleszynski Jayich, F. Jelezko, N. B. Manson, and M. W. Doherty, Nano Letters **17**, 1496 (2017).
[S6] A. Barfuss, M. Kasperczyk, J. Kölbl, and P. Maletinsky, Phys. Rev. B **99**, 174102 (2019).
[S7] P. Udvarhelyi, V. O. Shkolnikov, A. Gali, G. Burkard, and A. Pályi, Phys. Rev. B **98**, 075201 (2018).
[S8] M. W. Doherty, F. Dolde, H. Fedder, F. Jelezko, J. Wrachtrup, N. B. Manson, and L. C. L. Hollenberg, Phys. Rev. B **85**, 205203 (2012).
[S9] A. M. Glazer, J. G. Lewis, and W. Kaminsky, Proceedings of the Royal Society of London A: Mathematical, Physical and Engineering Sciences **452**, 2751 (1996).
[S10] W. Kaminsky, E. Gunn, R. Sours, and B. Kahr, Journal of Microscopy **228**, 153 (2007).
[S11] D. Howell, European Journal of Mineralogy **24**, 575 (2012).
[S12] D. Howell, I. G. Wood, F. Nestola, P. Nimis, and L. Nasdala, European Journal of Mineralogy **24**, 563 (2012).
[S13] D. Howell, I. G. Wood, D. P. Dobson, A. P. Jones, L. Nasdala, and J. W. Harris, Contributions to Mineralogy and Petrology **160**, 705 (2010).
[S14] A. M. Zaitsev, Optical Properties of Diamond: A Data Handbook (Springer, 2001).
[S15] Geday, Kaminsky, Lewis, and Glazer, Journal of Microscopy **198**, 1 (2000).

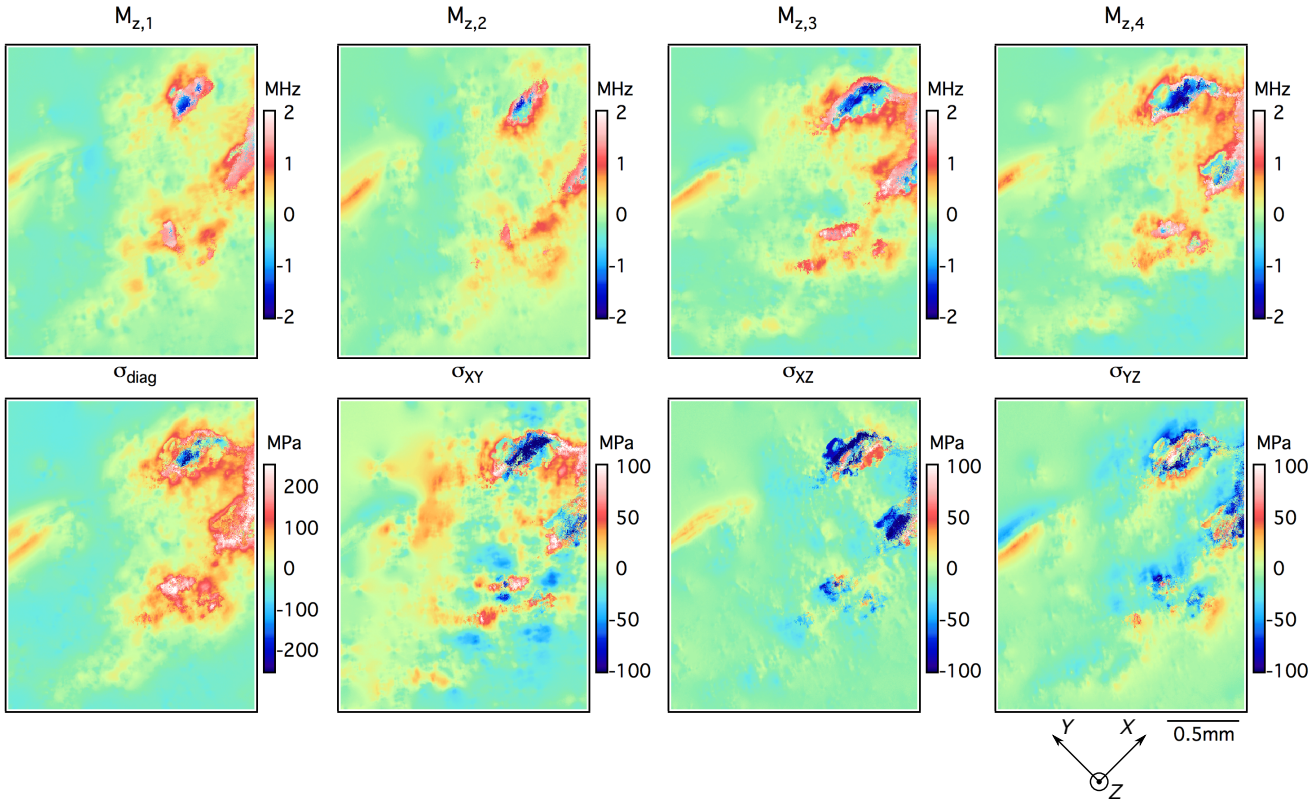
[S16] H. Pinto and R. Jones, Journal of Physics: Condensed Matter **21**, 364220 (2009).
[S17] I. Friel, S. Clewes, H. Dhillon, N. Perkins, D. Twitchen, and G. Scarsbrook, Diamond and Related Materials **18**, 808 (2009).
[S18] K. Ohno, F. J. Heremans, L. C. Bassett, B. A. Myers, D. M. Toyli, A. C. B. Jayich, C. J. Palmstrom, and D. D. Awschalom, Applied Physics Letters **101**, 082413 (2012).
[S19] H. Jasbeer, R. J. Williams, O. Kitzler, A. McKay, S. Sarang, J. Lin, and R. P. Mildren, J. Opt. Soc. Am. B **33**, B56 (2016).
[S20] M. W. Doherty, V. V. Struzhkin, D. A. Simpson, L. P. McGuinness, Y. Meng, A. Stacey, T. J. Karle, R. J. Hemley, N. B. Manson, L. C. L. Hollenberg, and S. Prawer, Phys. Rev. Lett. **112**, 047601 (2014).
[S21] H. Pinto, R. Jones, J. P. Goss, and P. R. Briddon, J. Phys.: Conf. Ser. **281**, 012023 (2011).



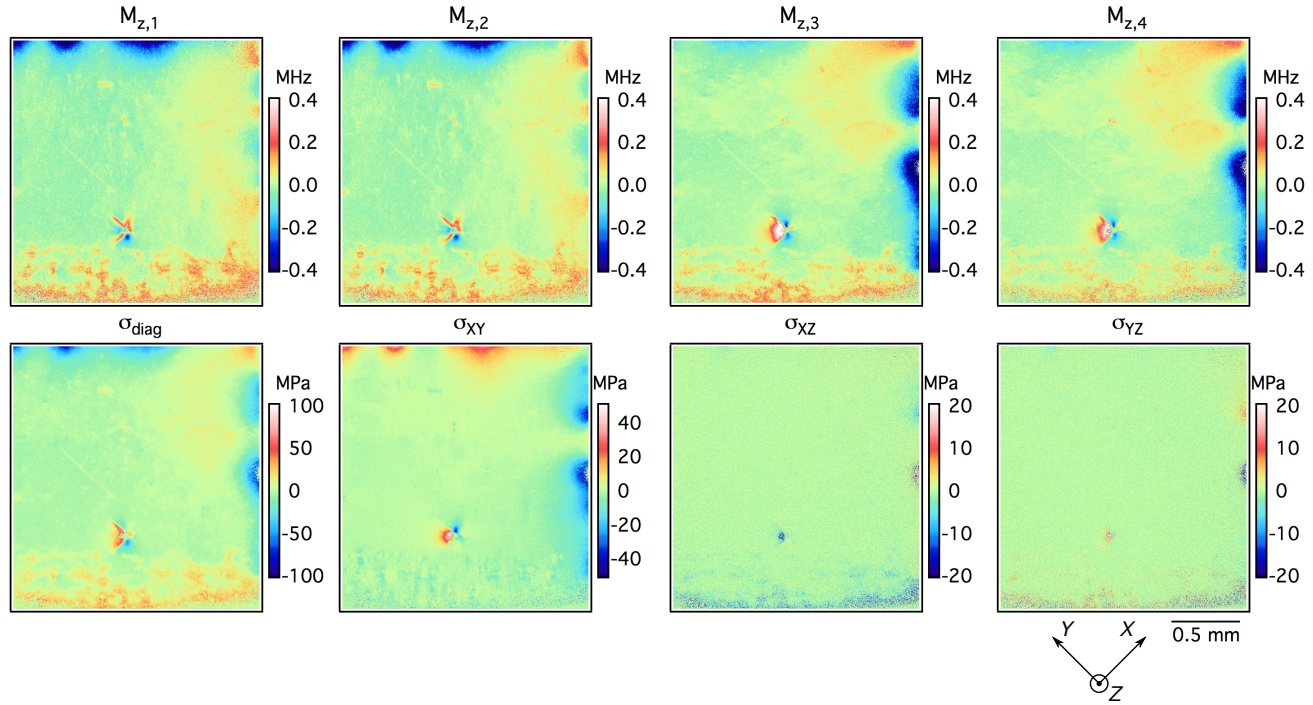
Supplemental Figure S10. NV $M_{z,\kappa}$ and $\{\sigma_{diag}, \sigma_{XY}, \sigma_{XZ}, \sigma_{YZ}\}$ maps for diamond Sample A. (Identical to Fig. 3 in the main text, but included here for completeness.)



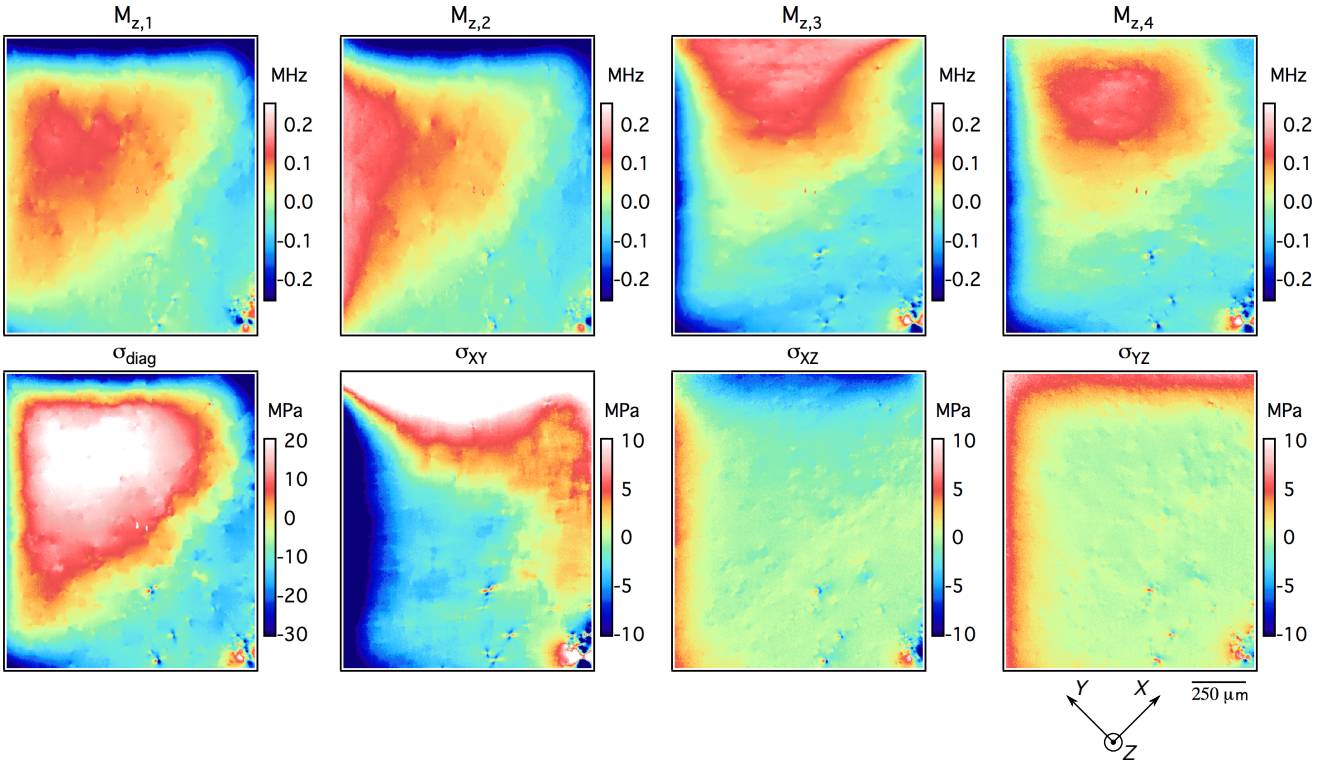
Supplemental Figure S11. NV $M_{z,\kappa}$ and $\{\sigma_{diag}, \sigma_{XY}, \sigma_{XZ}, \sigma_{YZ}\}$ maps for diamond Sample B.



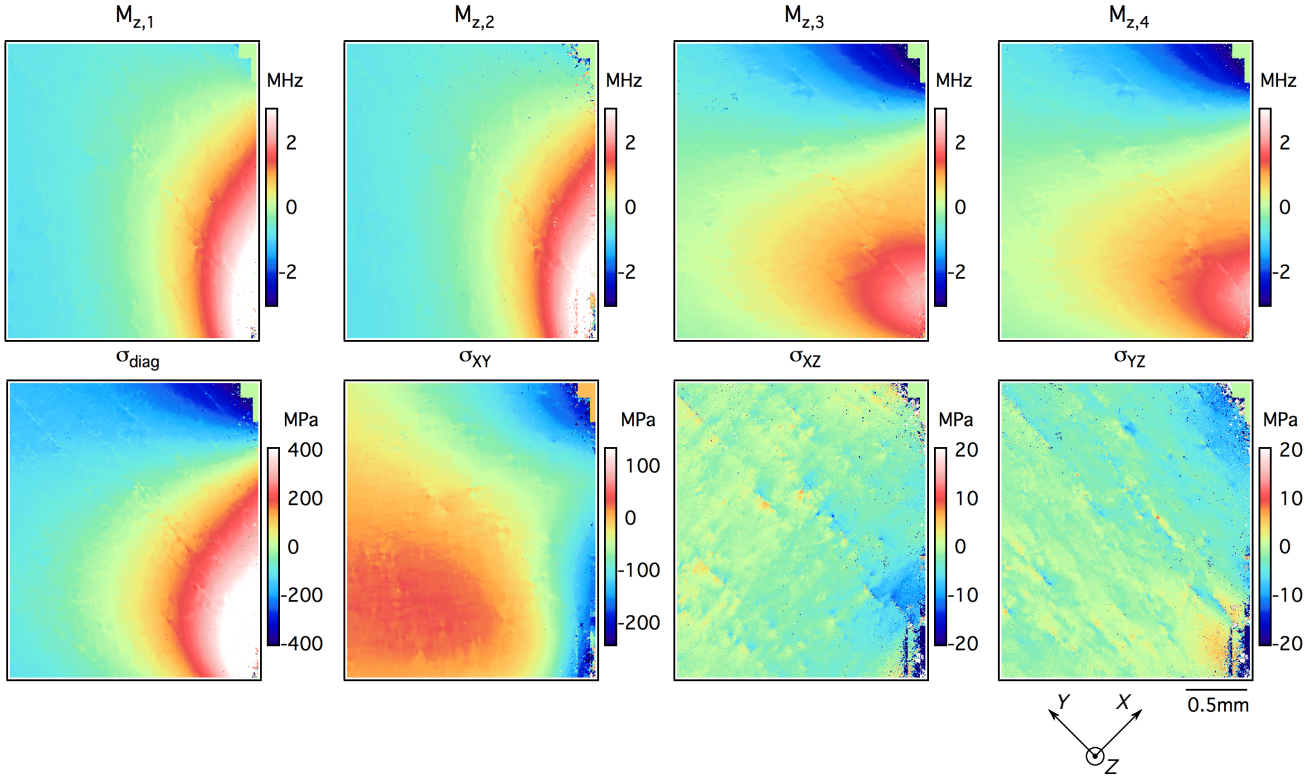
Supplemental Figure S12. NV $M_{z,\kappa}$ and $\{\sigma_{diag}, \sigma_{XY}, \sigma_{XZ}, \sigma_{YZ}\}$ maps for diamond Sample C.



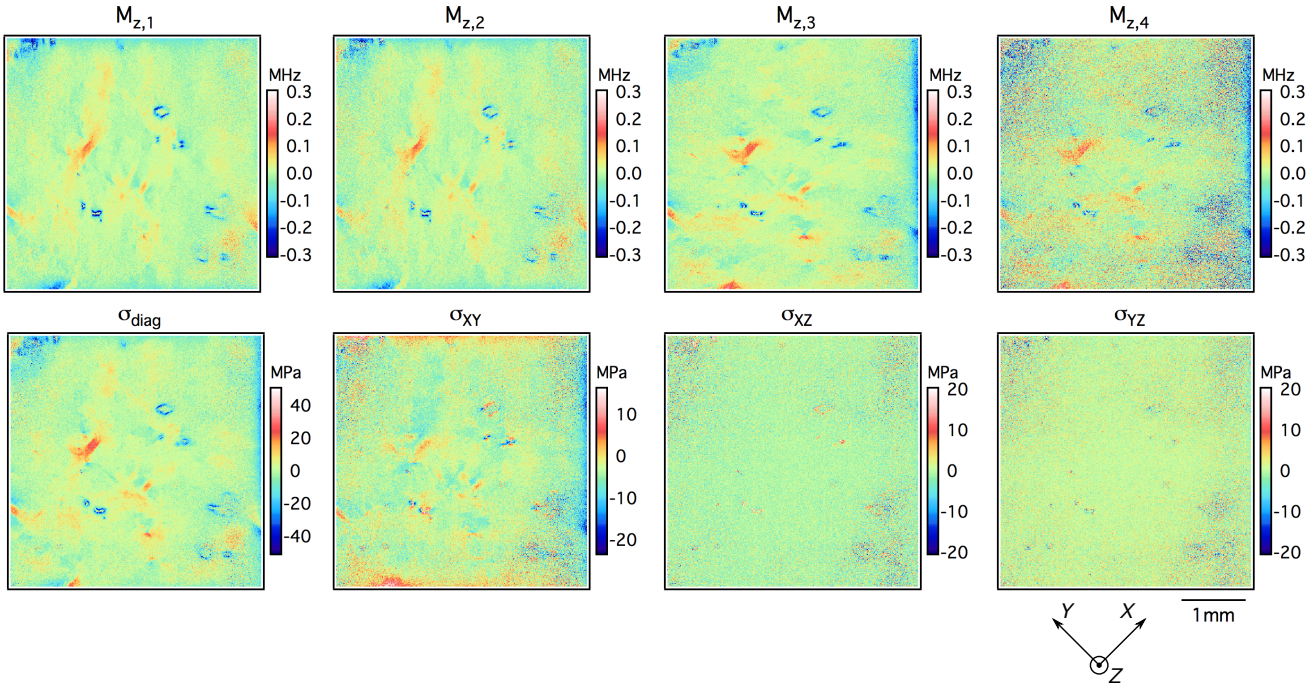
Supplemental Figure S13. NV $M_{z,\kappa}$ and $\{\sigma_{diag}, \sigma_{XY}, \sigma_{XZ}, \sigma_{YZ}\}$ maps for diamond Sample D.



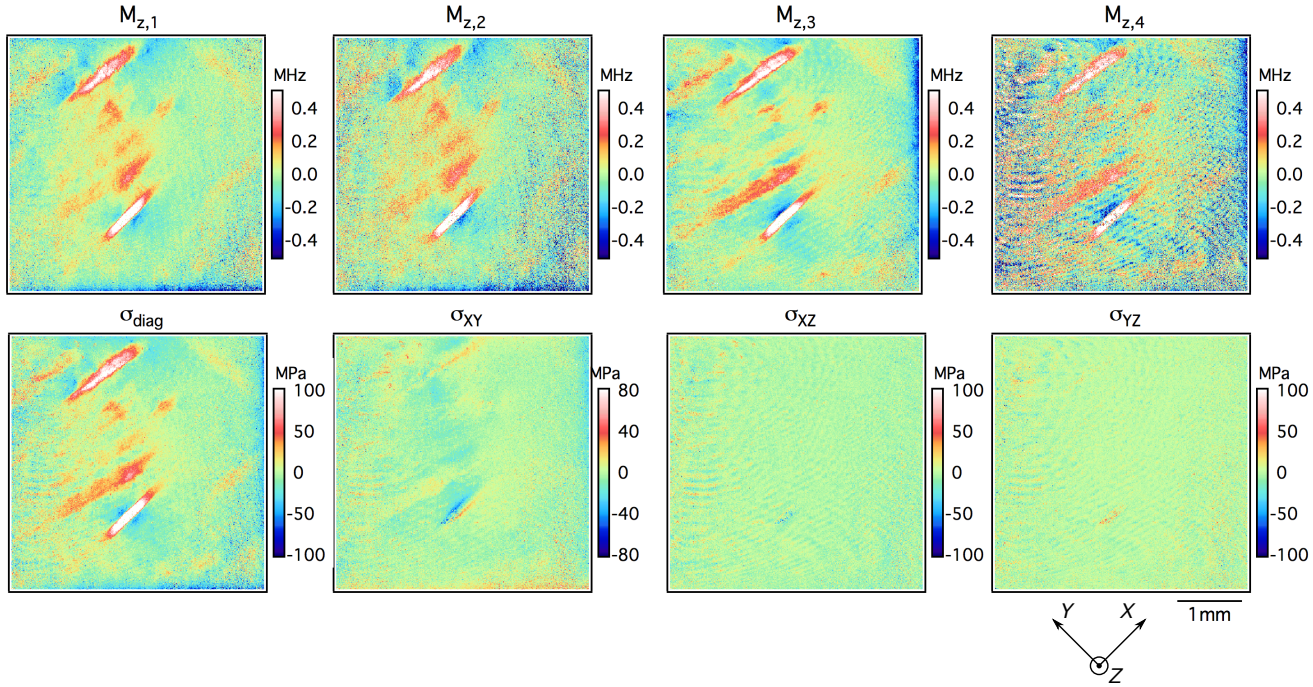
Supplemental Figure S14. NV $M_{z,\kappa}$ and $\{\sigma_{diag}, \sigma_{XY}, \sigma_{XZ}, \sigma_{YZ}\}$ maps for diamond Sample E.



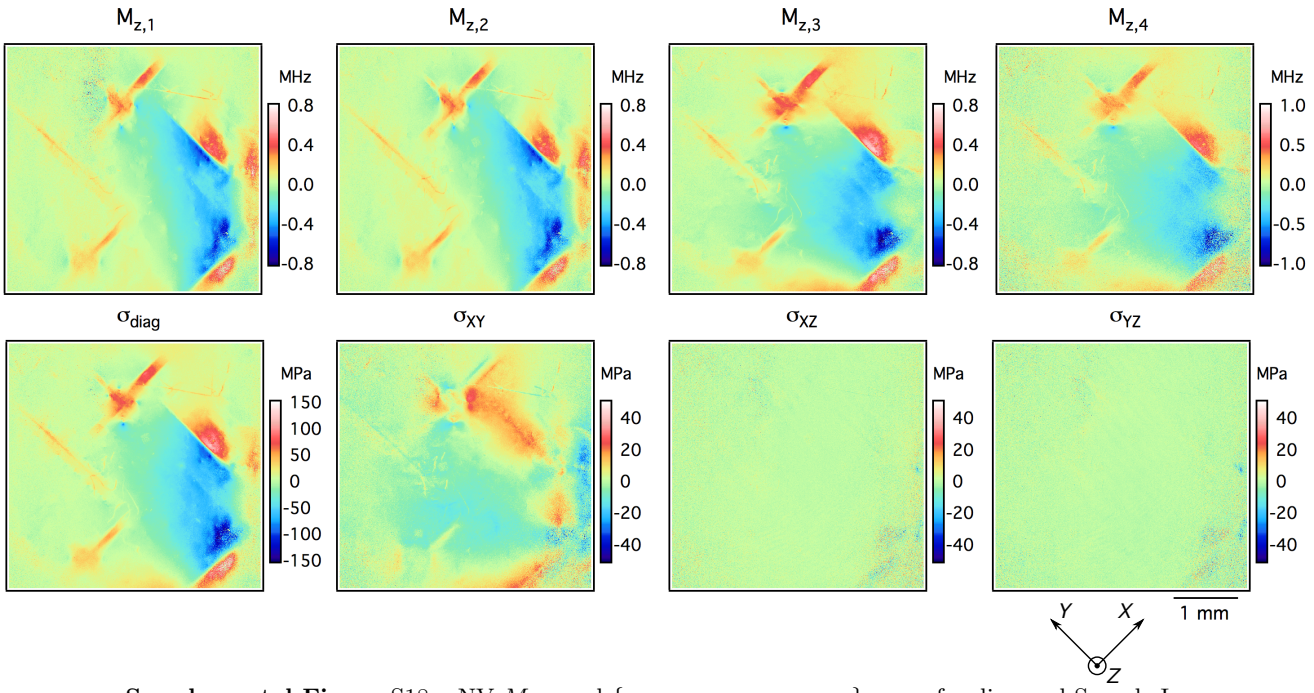
Supplemental Figure S15. NV $M_{z,\kappa}$ and $\{\sigma_{diag}, \sigma_{XY}, \sigma_{XZ}, \sigma_{YZ}\}$ maps for diamond Sample F.



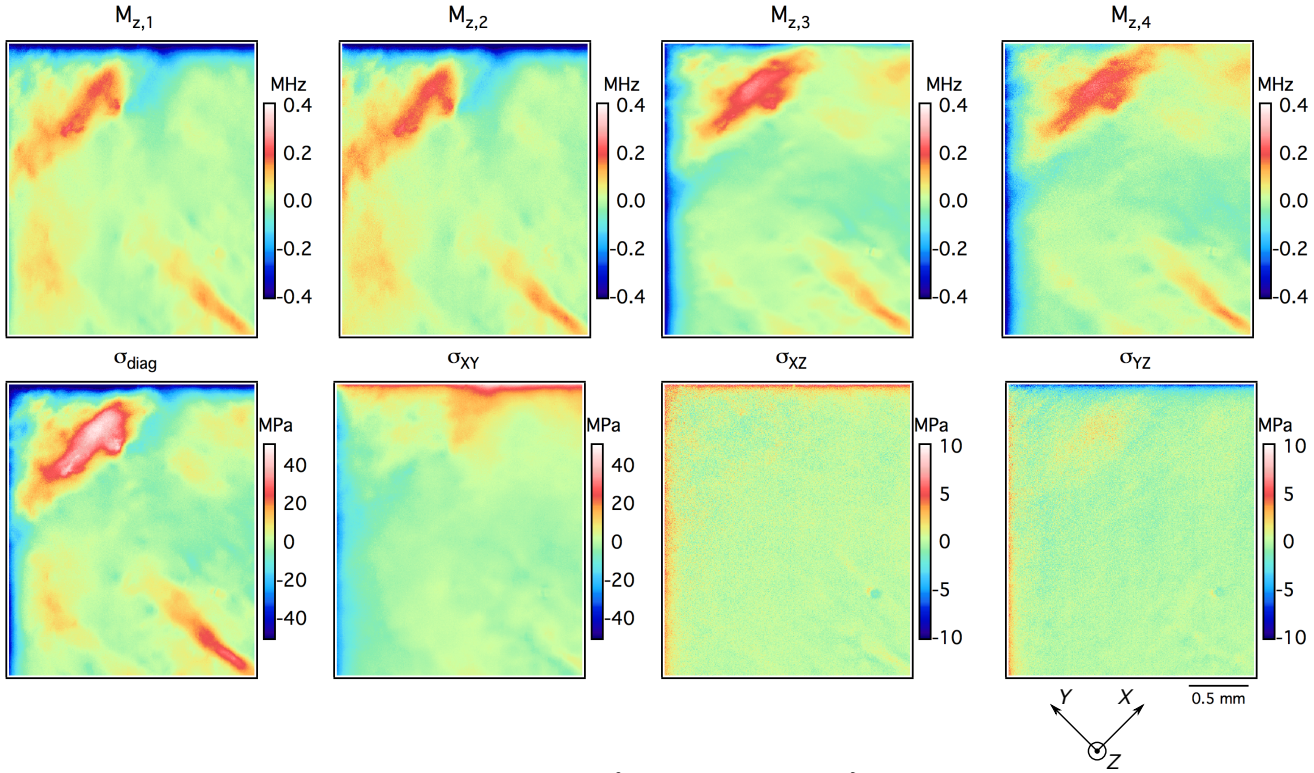
Supplemental Figure S16. NV $M_{z,\kappa}$ and $\{\sigma_{diag}, \sigma_{XY}, \sigma_{XZ}, \sigma_{YZ}\}$ maps for diamond Sample G.



Supplemental Figure S17. NV $M_{z,\kappa}$ and $\{\sigma_{diag}, \sigma_{XY}, \sigma_{XZ}, \sigma_{YZ}\}$ maps for diamond Sample H.



Supplemental Figure S18. NV $M_{z,\kappa}$ and $\{\sigma_{diag}, \sigma_{XY}, \sigma_{XZ}, \sigma_{YZ}\}$ maps for diamond Sample I.



Supplemental Figure S19. NV $M_{z,\kappa}$ and $\{\sigma_{diag}, \sigma_{XY}, \sigma_{XZ}, \sigma_{YZ}\}$ maps for diamond Sample J.